Electronic Supplementary Information

Solar-powered interfacial evaporation system based on MoS$_2$-decorated magnetic phase-change microcapsules for sustainable seawater desalination

Haohai Shen, Zhiheng Zheng, Huan Liu[*], Xiaodong Wang[*]

State Key Laboratory of Organic–Inorganic Composites, Beijing University of Chemical Technology, Beijing 100029, China.

* Corresponding authors.

 E-mail address: bucthuan@163.com (H. Liu), wangxdfox@aliyun.com (X. Wang);

Summary of Content

Section S1. Preparation of Fe_3O_4 nanoparticles.

Section S2. Characterizations and measurements.

Fig. S1. Schematic stripping process of MoS_2 nanosheets.

Fig. S2. SEM images of (a) MoS_2 powders and (b) MoS_2 multilayered nanosheets.

Fig. S3. Plots of particle-size distributions of (a) Fe_3O_4/SiO_2-MEPCM and (b) MoS_2-MEPCM.

Fig. S4. High-resolution core-level XPS spectra of Fe_3O_4/SiO_2-MEPCM.

Fig. S5. EDX pattern and elemental mapping images of Fe_3O_4/SiO_2-MEPCM.

Fig. S6. Mass change of MoS_2-MEPCM in the water body at 50 ºC.

Fig. S7. Water mass changes of MoS_2-MEPCM evaporator during the cyclic washing process.

Fig. S8. UV-Vis-NIR absorption spectra of MoS_2-MEPCM after washing ten times.

Fig. S9. DSC thermograms of the MoS_2-MEPCM obtained after every washing process.

Fig. S10. Phase-change parameters of MoS_2-MEPCM obtained after every washing process.

Fig. S11. FTIR spectra of MoS_2-MEPCM before and after the recycling experiment.

Fig. S12. XRD patterns of MoS_2-MEPCM before and after the recycling experiment.

Fig. S13. Water evaporation production of MoS_2-MEPCM-based evaporator during 15 days of natural sunlight illumination.

Fig. S14. Evaporation rate of MoS_2-MEPCM-based evaporator during 15 days of natural sunlight illumination.

Table S1. Detection results of water quality for purified water.

Section S1. Preparation of Fe₃O₄ nanoparticles.

The synthetic process of Fe_3O_4 nanoparticles was prepared as follows: $FeCl_2 \cdot 4H_2O$ (0.078 mol L^{-1}, 50.0 mL) and $FeCl_3 \cdot 6H_2O$ (0.046 mol L^{-1}, 50.0 mL) solutions were mixed in a three-necked round bottom flask (250 mL) with stirring under a nitrogen atmosphere at 25 ºC for 30 min. $NH_3 \cdot H_2O$ (4.0 mL, 25 wt%) was added in the flask with continuous stirring at 25 ºC for 1 h. With the reaction completed, the Fe_3O_4 nanoparticles were separated from the resultant mixture solution by a magnet, washed with deionized water and formamide for three times, and dispersed in formamide (100 mL).

Section S2. Characterizations and Measurements.

The morphology of MoS_2 nanosheets and phase-change microcapsules was characterized by a field emission scanning electron microscope (SEM, SU8020, Hitachi, Japan) with an acceleration voltage of 15 kV. The SEM equipped with an energy-dispersive X-ray (EDX) spectrometer (INCAX-Act, Oxford, UK) was employed to analyze the surface elemental composition and mapping images of phase-change microcapsules. The microstructure of MoS_2 nanosheets and phase-change microcapsules was observed by a field emission transmission electron microscope (TEM, JEM-2100F, JEOL, Japan) operated with an accelerating voltage of 200 kV, and the selected area electron diffraction (SAED) of MoS_2 nanosheets was characterized by the same instrument. The *Fourier*-transform infrared (FTIR) spectra of pure *n*-docosane and phase-change microcapsules were determined by an infrared spectrometer (Nicolet iS5, Thermo Scientific, USA). The X-ray diffraction (XRD) pattern was characterized by X–ray diffractometer (D/max 2500, Rigaku, Japan) at 40 mA and 40 kV with Cu Kα radiation (λ =1.5418 Å) and a scan speed of 10° min^{-1}. The X-ray photoelectron spectroscopy (XPS) analysis of phase-change microcapsules was carried out through X–ray photoelectron spectrometer (ESCALAB 250Xi, Thermo Scientific, USA) equipped with a focused monochromatized Al Kα radiation source. The shape stability of pure *n*-docosane and phase-change microcapsules was characterized by heating on a high-precision electronic hot plate at 120

ºC. The appearances of the samples were monitored by a digital camera. Thermal analysis was performed to evaluate the phase-change behavior of pure n-docosane and phase-change microcapsules by a differential scanning calorimeter (DSC, Q20, TA Instruments, USA) under a ramp rate of 10 ºC min^{-1}. Phase-change temperatures, including melting temperature (T_m, °C), crystallization temperature (T_c, ºC), and rotator phase-transition temperature (T_R, °C) were directly obtained from the DSC thermograms. Phase-change enthalpies, including melting enthalpy (ΔH_m, J g^{-1}) and crystallization enthalpy (ΔH_c, J g^{-1}) were obtained by integrating the endothermic and exothermic peaks in the DSC thermograms. The encapsulation parameters were determined by the phase-change enthalpies based on the following equations.

$$E_{en}(\%) = \frac{\Delta H_{m,\,microcapsules}}{\Delta H_{m,\,docosane}} \times 100\% \tag{1}$$

$$E_{es}(\%) = \frac{\Delta H_{m,\,microcapsules} + \Delta H_{c,\,microcapsules}}{\Delta H_{m,\,docosane} + \Delta H_{c,\,docosane}} \times 100\% \tag{2}$$

$$C_{es}(\%) = \frac{(\Delta H_{m,\,microcapsules} + \Delta H_{C,\,microcapsules}) \cdot \Delta H_{m,\,docosane}}{(\Delta H_{M,\,docosane} + \Delta H_{C,\,docosane}) \cdot \Delta H_{M,\,microcapsules}} \times 100\% \tag{3}$$

where E_{en} (%) is the encapsulation ratio, E_{es} (%) is the energy-storage efficiency, C_{es} (%) is the energy-storage capability, $\Delta H_{m,\,docosane}$ (J g^{-1}) and $\Delta H_{c,\,docosane}$ (J g^{-1}) are the melting enthalpy and crystallization enthalpy of pure n-docosane, respectively, and $\Delta H_{m,\,microcapsules}$ (J g^{-1}) and $\Delta H_{c,\,microcapsules}$ (J g^{-1}) are the melting and crystallization enthalpies of phase-change microcapsules, respectively. The thermal conductivity was characterized by a thermal conductivity tester (HS-DR-5, HESHENG, China) with an accuracy of ± 3%. The dynamic water contact angle was measured by a water angle measuring instrument (JY-82C, Dingsheng, China) with a water droplet volume of 16 μL. The absorption spectra of phase-change microcapsules were characterized by an UV-Vis-NIR spectrophotometer (UV-3600Plus, Shimadzu, Japan) with a test range of 220−2,500 nm. The photothermal conversion performance was evaluated by a Xenon arc lamp as a light source (Irradiation intensity: 1000 W m^{-2}). The temperature evolution during the photothermal conversion process was determined by a k-type thermocouple.
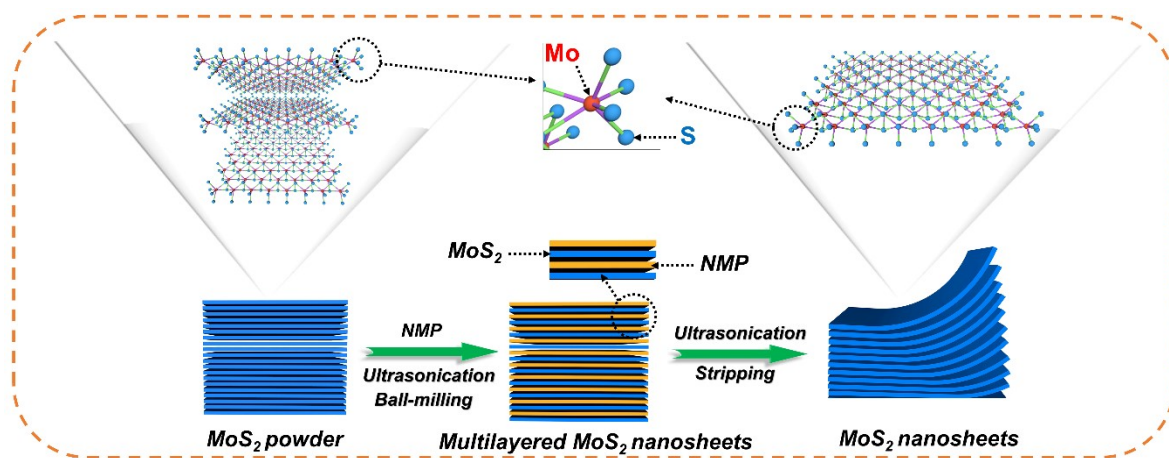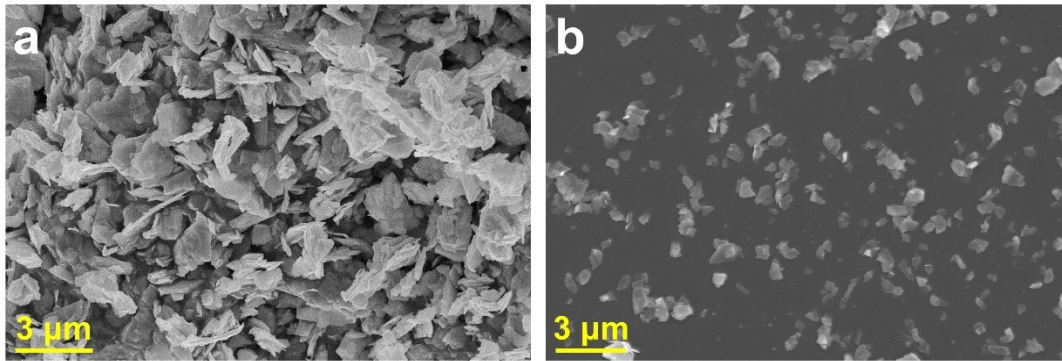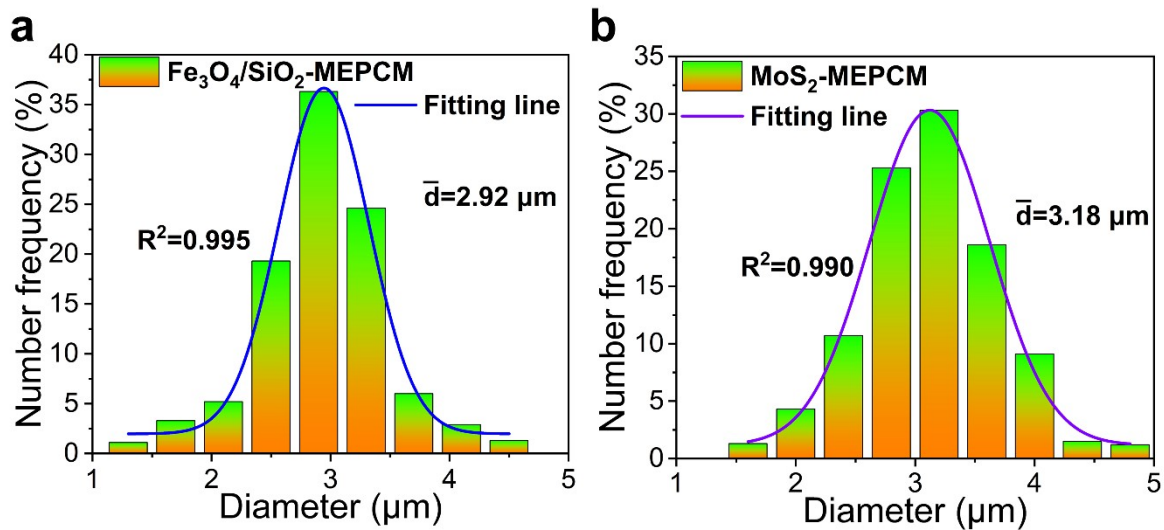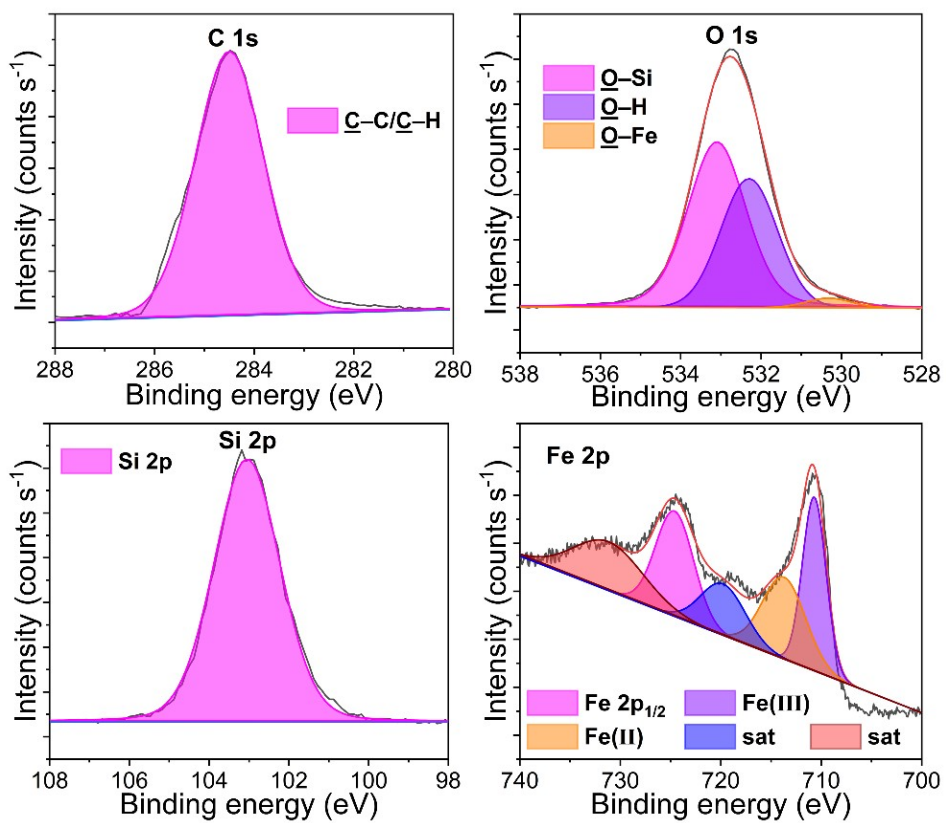
Fig. S1. Schematic stripping process of MoS_2 nanosheets.

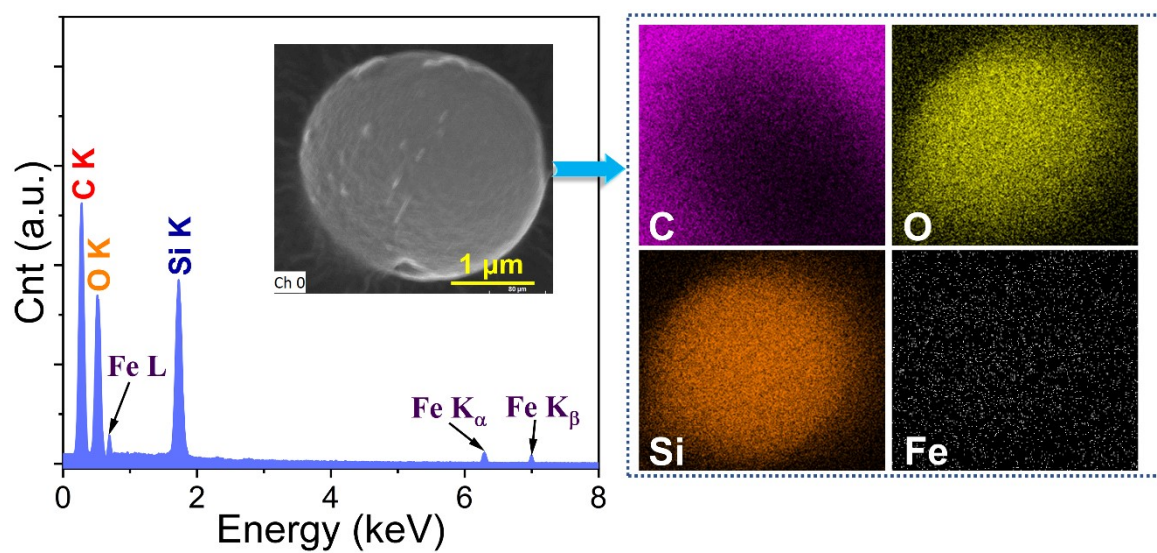**Fig. S2.** SEM images of (a) MoS_2 powders and (b) MoS_2 multilayered nanosheets.

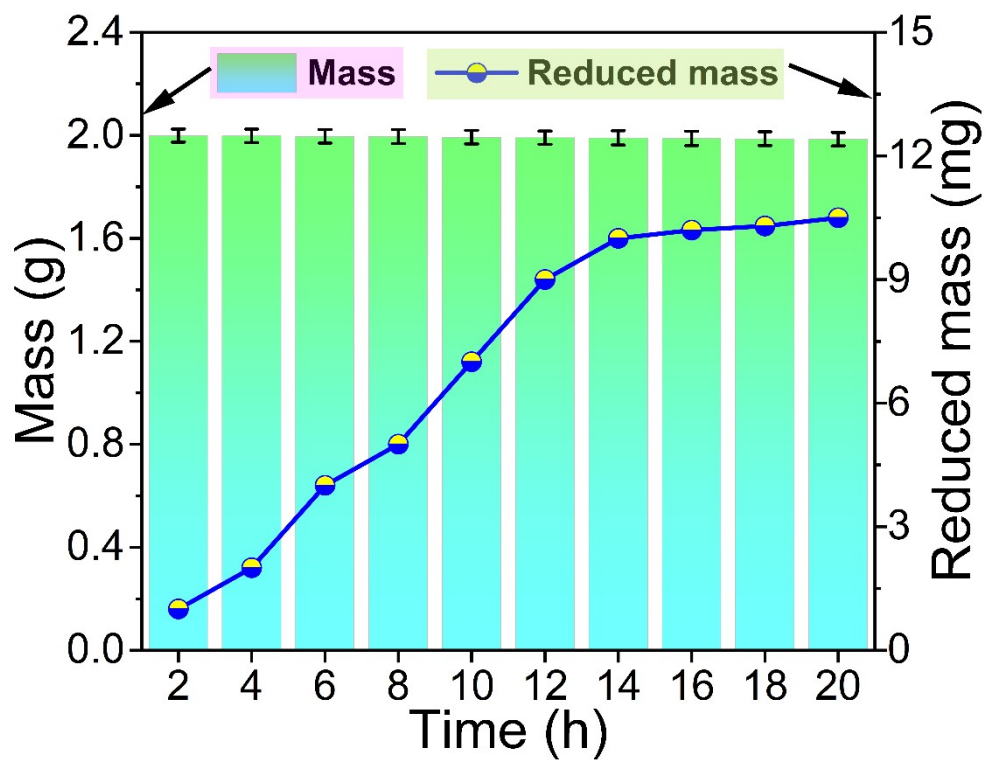**Fig. S3.** Plots of particle-size distribution of (a) Fe_3O_4/SiO_2-MEPCM and (b) MoS_2-MEPCM.

Fig. S4. High-resolution core-level XPS spectra of Fe_3O_4/SiO_2-MEPCM.

Fig. S5. EDX pattern and elemental mapping images of Fe_3O_4/SiO_2-MEPCM.

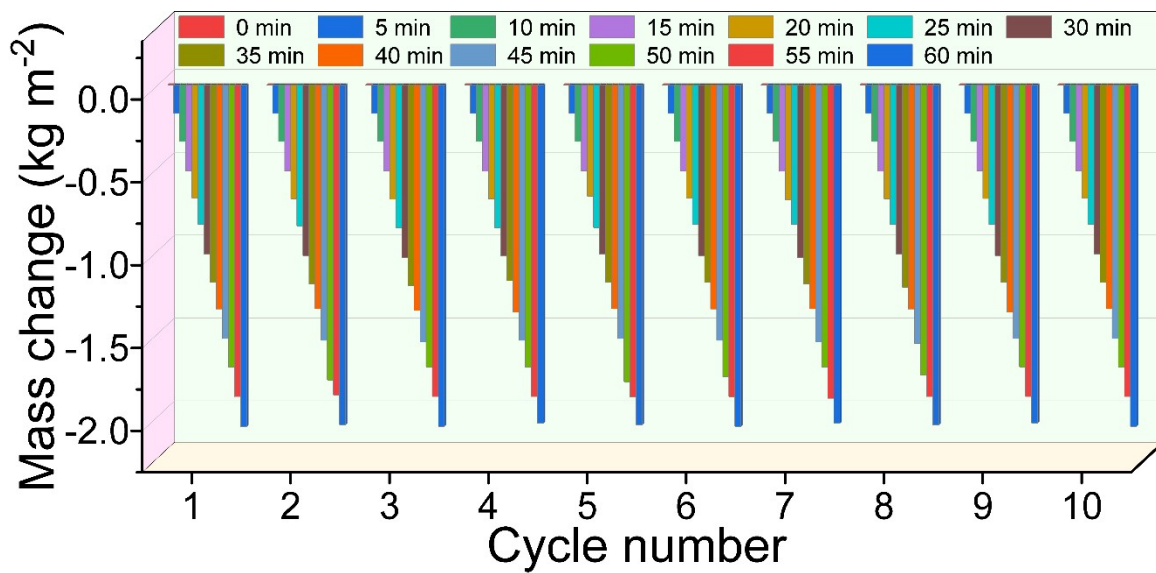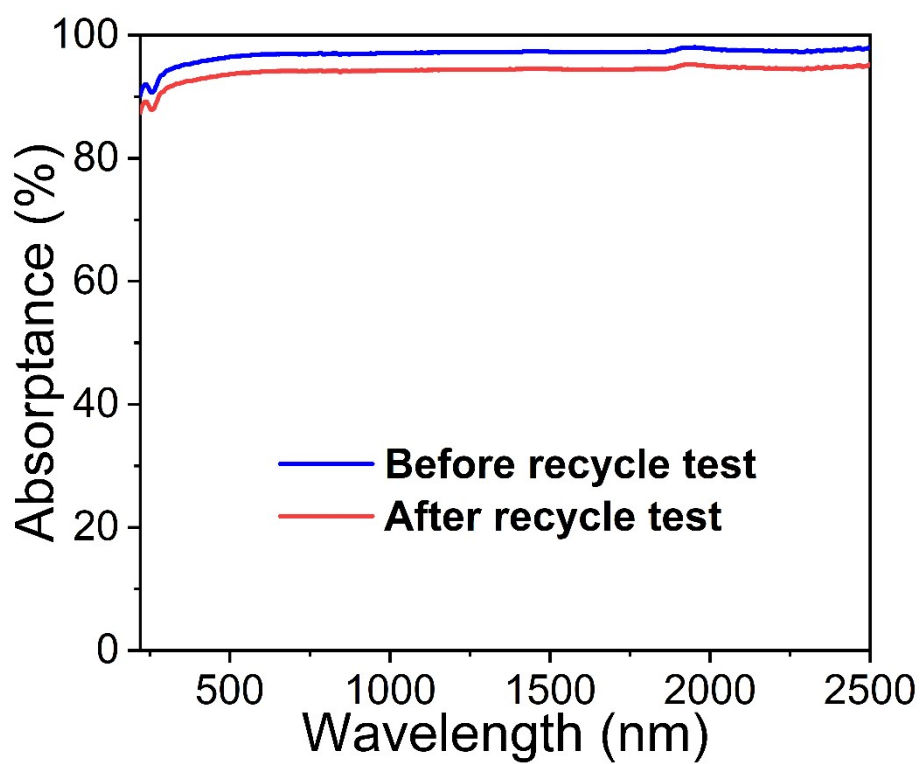**Fig. S6.** Mass change of MoS$_2$-MEPCM in the water body at 50 °C.

Fig. S7. Mass change of MoS$_2$-MEPCM evaporator during the cyclic washing process.

Fig. S8. UV-Vis-NIR absorption spectra of MoS$_2$-MEPCM before and after the recycling

experiment.

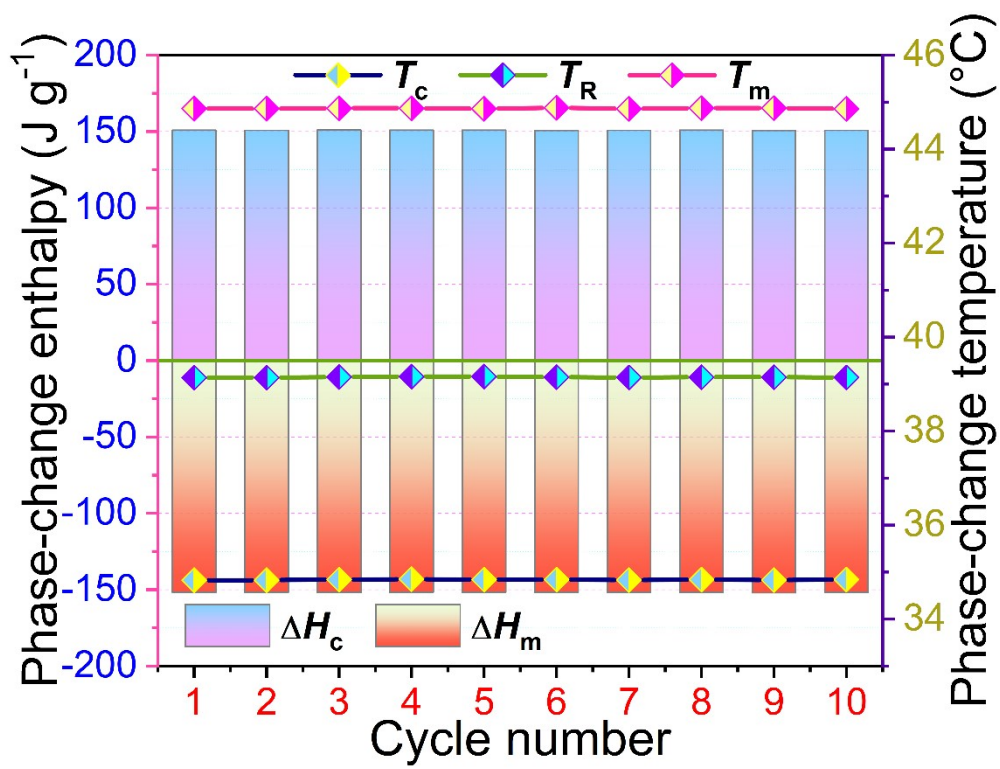**Fig. S9.** DSC thermograms of the MoS$_2$-MEPCM obtained after every washing process.

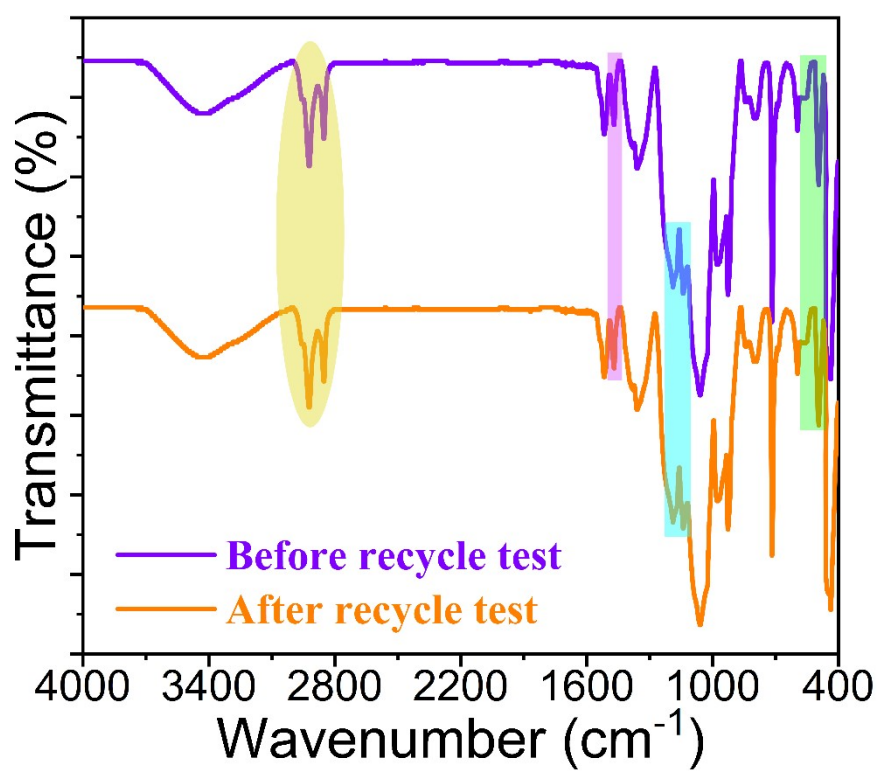**Fig. S10.** Phase-change parameters of MoS_2-MEPCM obtained after every washing process.
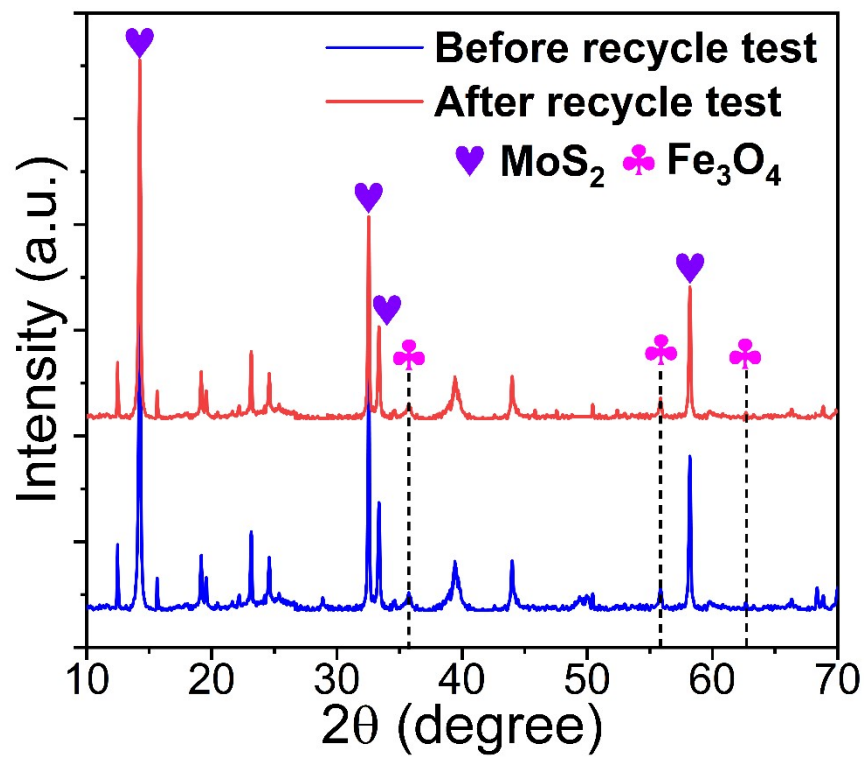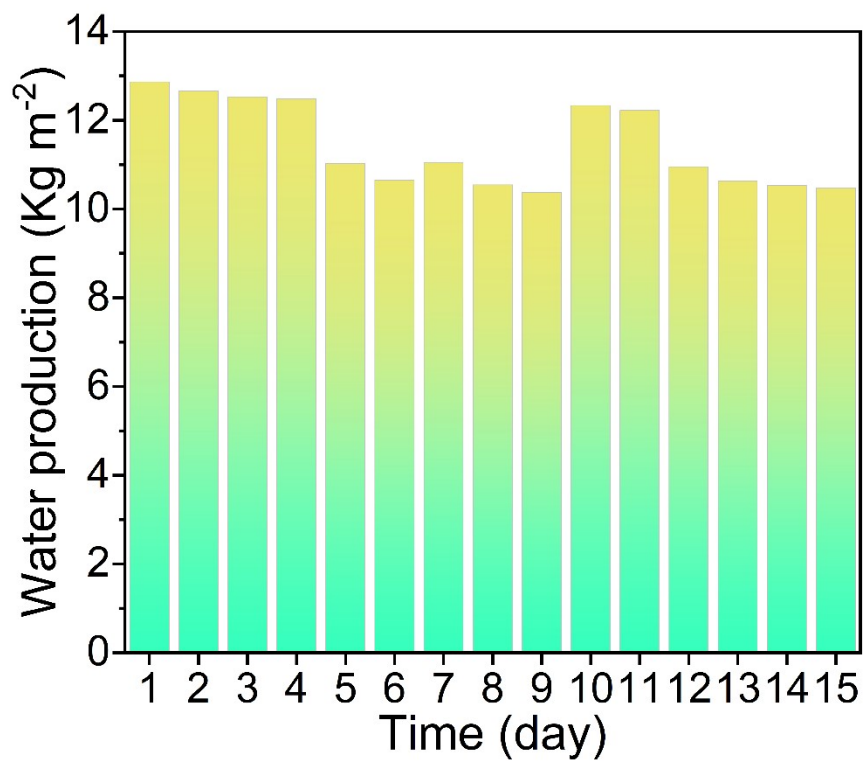
Fig. S11. FTIR spectra of MoS_2-MEPCM before and after the recycling experiment.
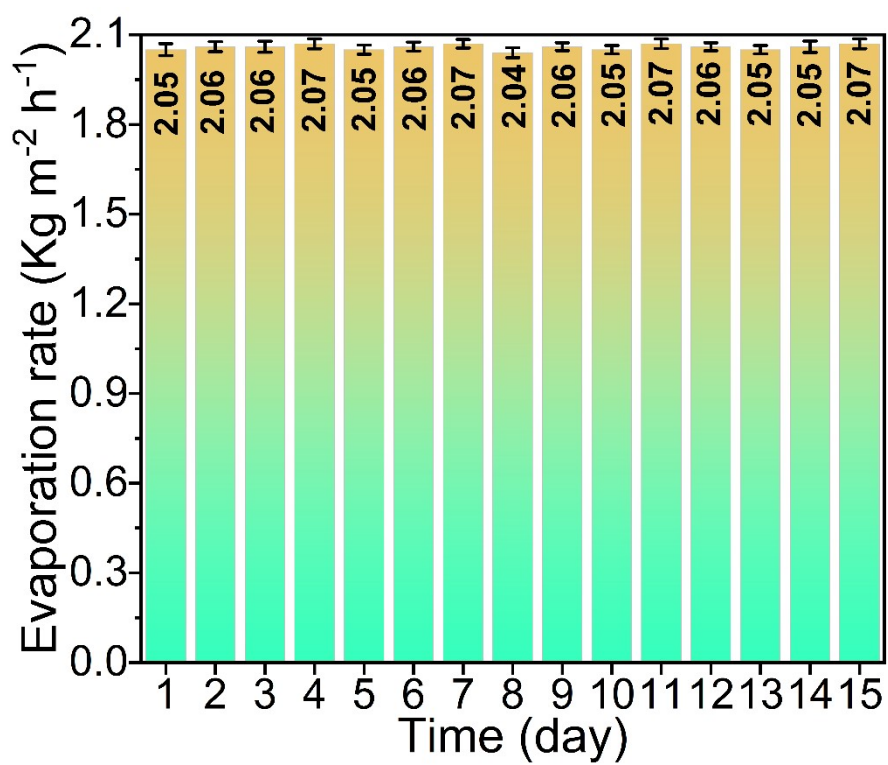
Fig. S12. XRD patterns of MoS$_2$-MEPCM before and after the recycling experiment.

Fig. S13. Water evaporation production of MoS_2-MEPCM-based evaporator during 15 days of natural sunlight illumination.

Fig. S14. Evaporation rate of MoS_2-MEPCM-based evaporator during 15 days of natural sunlight illumination.

Table S1. Detection results of water quality for purified water

Detection item	Numerical value
Anion synthetic detergent (mg L^{-1})	< 0.1
Volatile organic compound (mg L^{-1})	< 0.002
Coliform colony (L^{-1})	Not detected
pH value	6.95